Astron. Astrophys. 342, 839–853 (1999)

ASTRONOMY AND ASTROPHYSICS

ROSAT PSPC observation of the NE region of the Vela supernova remnant

III. The two-component nature of the X-ray emission and its implications on the ISM

F. Bocchino, A. Maggio, and S. Sciortino

Osservatorio Astronomico di Palermo "G.S. Vaiana", Palazzo dei Normanni, I-90134 Palermo, Italy

Received 13 July 1998 / Accepted 13 October 1998

Abstract. We reconsider two *ROSAT* observations of the Vela SNR shock region, with the aim to overcome the problems encountered in interpreting the X-ray spectra in terms of single-temperature NEI emission model. We pursue the idea of the association of the observed cool and hot components with an high-density ("inhomogeneities") and a low-density ("intercloud") ISM phase, respectively. We derive the density (0.5–1.0 cm^{-3}) and the volume filling factor (0.2–0.8) of the inhomogeneities on a scale length of $10'$ (~ 1 pc), and we identify two regions of the main shock interactions, one with a small ($\sim$ 1 pc) isolated cloud, and the other with a larger feature ($\sim$ 4–5 pc, perhaps a cavity wall). We argue that the thermal evaporation from shocked clouds may account for the mass of observed inhomogeneities. After isolating the emission of the dynamically unperturbed intercloud medium, we apply the Sedov analysis and estimate the explosion energy of the supernova event ($E_0 \sim 1.2 \times 10^{50}$ erg) and the distance (~ 280 pc, in agreement with recent results). Our data also indicate fast electron-ion equipartition behind the shock. The influence of Non-Equilibrium of Ionization effects on our conclusions are estimated.

Key words: X-rays: ISM – ISM: supernova remnants – ISM: structure – ISM: individual objects: Vela supernova remnant – ISM: general – ISM: clouds

1. Introduction

This is the third paper of a series dedicated to *ROSAT* pointed PSPC observations of the Vela supernova remnant (SNR) shock region. In this series, we have taken advantage of the moderate PSPC spatial and spectral resolution to carry out a spatially resolved spectral analysis of the X-ray emission in the 0.2–2.0 keV band. The region we have analyzed has an area of ~ 3 square degrees, 8% of the total extension of the Vela SNR X-ray emission as measured by the *ROSAT* All-Sky Survey (Aschenbach 1993). In Bocchino et al. (1994, Paper I), we showed that a single-temperature thermal emission model in Collisional Equilibrium of Ionization (hereafter the 1T CIE model), such as the one described in Raymond & Smith (1977), does not give an adequate description of the data. This is an important result because, even though the plasma in SNR's is expected to be in Non Equilibrium of Ionization (NEI, Itoh 1979), the 1T CIE model was extensively used in the past to describe the X-ray emission of the Vela SNR (Kahn et al. 1985). At the same time, we pointed out that the spectral features of the X-ray emission change noticeably at the explored scale length of ~ 0.4 pc. In Paper I, we also noted that a two-temperature Raymond & Smith (1977) thermal emission model in CIE condition (2T CIE) fits satisfactory the data, but, following Itoh (1979), we suggested that this result could be attributed to NEI effects and to the moderate PSPC spectral resolution; for this reason, we did not interpret the fitting results as an evidence of two distinct components in the emitting plasma. In Bocchino et al. (1997, Paper II), we developed and tested a single-temperature – single-ionization time NEI emission model for fitting the PSPC data (hereafter the STNEI model), and we found that in order to achieve a satisfactory fit, the ionization time had to be unreasonably low ($< 10\,\mathrm{yr\,cm}^{-3}$). The difficulty to find a physical explanation for this result led us to reconsider multi-component emission models as a feasible description of the Vela SNR X-ray emission. In particular, we argued that the failure of a single-temperature model (either in CIE or in NEI conditions) and the success of a two-temperature model in describing the data might reflect the intrinsic nature of the post-shock plasma, and may indicate, for instance, the presence of inhomogeneities in the swept up interstellar medium. In this paper, we intend to explore this possibility, and we shall show that this interpretation is not only consistent with the observational evidences, but also it provides us with insights on the local ISM structure.

The paper is organized as follows. In Sect. 2 we present the data, in Sect. 3 we outline the results of the application of the two-temperature model, while in Sect. 4 we discuss the interpretation of the thermal components and we estimate the remnant and ISM characteristic parameters. We summarize our achievements in Sect. 5.

Send offprint requests to: bocchino@oapa.astropa.unipa.it

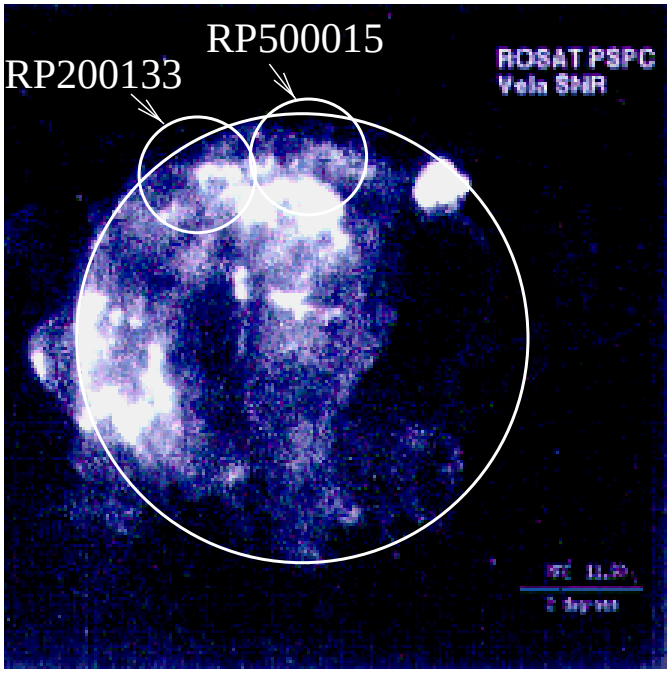

Fig. 1. The Vela SNR in the *ROSAT* 0.1–2.4 keV All-Sky Survey. Small circles mark the position of the PSPC sequences RP200133 and RP500015, whereas the large 3.6° radius circle encloses the Vela SNR diffuse emission (adapted from Aschenbach 1993).

Table 1. The RP200133 and RP500015 PSPC sequences

Name	RA (2000)	Dec (2000)	t_{uscr} - t_{scr} (%)[1]a[a]	N_{ph}[b]
RP200133	$8^h44^m24^s$	$-42°39'00''$	3944–3760 (5%)	5×10^5
RP500015	$8^h34^m43^s$	$-42°26'24''$	10304–9796 (5%)	18×10^5

[a] We report the exposure time before and after the application of the time screening algorithm of Bocchino et al. (1998).
[b] Number of counts in the whole field of view.

2. The data

Two pointed X-ray observations of the North and North-East rim of the Vela supernova remnant have been carried out with the Position Sensitive Proportional Counter on-board *ROSAT* (Trümper 1983). Table 1 summarizes the relevant information about the two sequences (RP200133 and RP500015). RP200133 (PI Sciortino) has been already studied in Paper I and in Paper II, while the public archive sequence RP500015 (PI Kahn) has been chosen to extend the coverage of the Vela outer shell in our spatially resolved spectral analysis. We recall that the PSPC has a circular field of view of $\sim 2°$ diameter, and its spatial resolution is $\sim 30''$ FWHM on axis and $\sim 2.5'$ FWHM at $45'$ off-axis, while the spectral resolution is $E/\Delta E \sim 2$ at 1 keV. Fig. 1 shows the *ROSAT* All-Sky Survey observation of the Vela SNR, with the position of the two sequences over-imposed. In order to remove high background time intervals from the X-ray observation, we have run the optimized time-screening algorithm of Bocchino et al. (1998) on both sequences: in Table 1 we report the screened and unscreened exposure times. The exposure maps have been recomputed according to the procedure of Snowden et al. (1994). The spatial grid used for spatially resolved spectral analysis consists of *sectors* and *rings* (Fig. 2), and was introduced in Paper II for RP200133. In particular, the outermost ring corresponds to the 3.6° radius circle introduced by Aschenbach (1993, also reproduced in Fig. 1), which encloses the Vela SNR diffuse emission.

3. Results

3.1. X-ray emission morphology

The two PSPC images are pointed toward the rim of the Vela shell, and therefore they are the least affected by the pulsar emission. To properly describe and classify the X-ray emission morphology, we divided the shell in three main regions, according to the observed surface brightness l_s in the energy band 0.2–2.0 keV:

Clumps: $l_s > 4.0 \times 10^{-2}$ cnt s^{-1} arcmin^{-2}. The clumps are the brightest regions in Fig. 1, and are irregularly distributed in the Vela SNR. They have been interpreted as tracer of inhomogeneities (e.g. Aschenbach 1993).

Diffuse emission: $1.0 \times 10^{-2} < l_s < 4.0 \times 10^{-2}$ cnt s^{-1} arcmin^{-2}. This range of l_s identifies the diffuse emission probably associated with the propagation of the shock in a medium less dense than the clumps, which are embedded in it.

Background: $l_s < 1.0 \times 10^{-2}$ cnt s^{-1} arcmin^{-2}. This is considered *background* emission, although it could not be necessarily associated with the cosmic background. Aschenbach (1993) pointed out that part of this emission could be associated with the remnant itself (see also Paper I).

In Paper I two major clumps were identified in the image of RP200133, named zone A (bin $d5$, $c5$, $d4$ $c4$ in the left panel of Fig. 2) and zone B (bins $b4$ and $b3$). In the outermost rings (6 and 7) few weaker structures are visible, like the filament in $b6$ (here classified as diffuse emission). For further details on the X-ray morphology of the part of the shell in RP200133, see Paper I.

The X-ray surface brightness in the image of RP500015 (Fig. 2, right panel) has a spatial distribution quite different from that of RP200133. In particular, it is possible to locate two separate "fronts", namely Front 1, the brightest of the two (classified as clump), placed nearer to the center of the remnant, and Front 2 (classified as diffuse emission), more external. Both fronts partially follow the grid curvature (in sector h, i and j, ring 1 for the Front 1 and ring 4 for the Front 2), and they show features at smaller scales. Between the two fronts, the surface brightness is low (typically classified as diffuse emission), except in sector k and j, where a bridge links Front 1 with Front 2. Like in the image of RP200133, most of the spatial bins in ring 7 include only background emission.

In the bin $l3$, there is a strong X-ray enhancement which we shall call Filament D (FilD). In FilD, the observed count rate

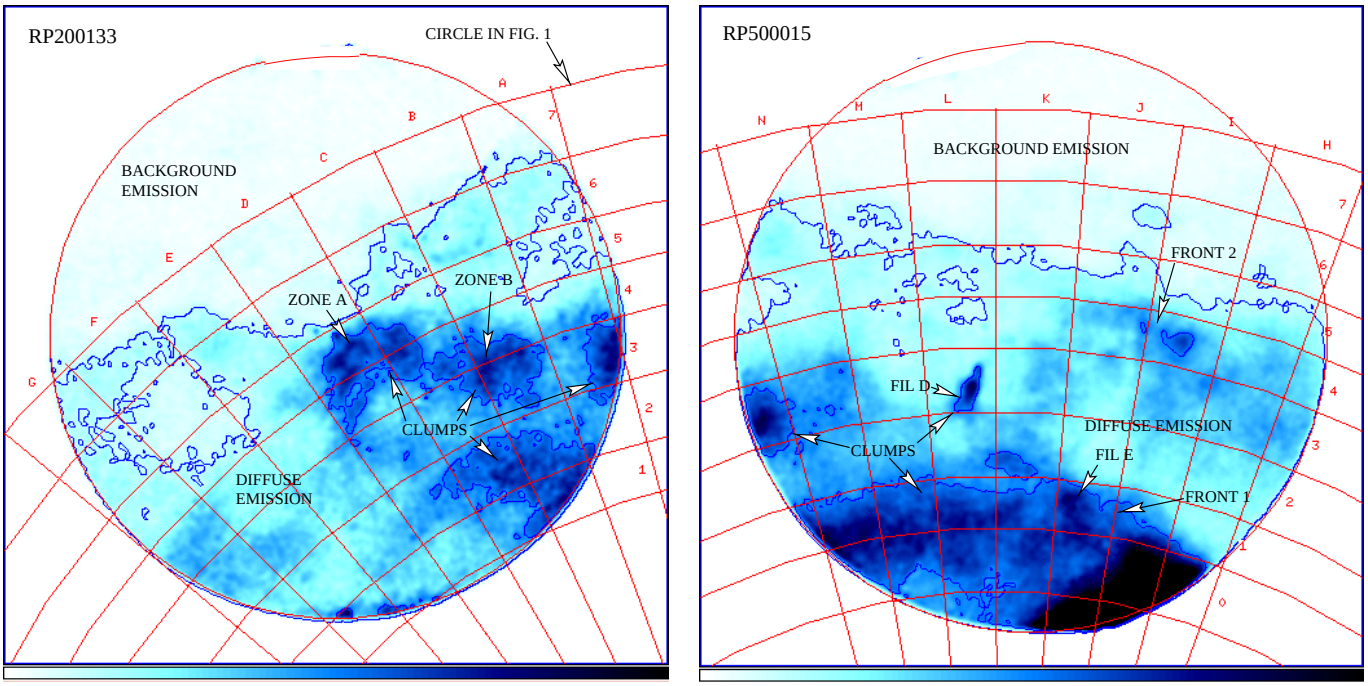

Fig. 2. Spatial distribution of 0.2–2.0 keV surface brightness of RP200133 (*left panel*) and RP500015 (*right panel*) PSPC sequences. 1.0 and 4.0 $\times 10^{-2}$ cnt s^{-1} arcmin^{-2} contours which marks the background, diffuse emission and clumps regions defined in Sect. 3.1 are overlaid. Grayscale is linear from 0 to 8.0 $\times 10^{-2}$ cnt s^{-1} arcmin^{-2}. North is up and East is on the left.

is 3–5 times higher than in surrounding regions. This feature is almost aligned in the North-South direction with an extension of $\sim 7'$, while its dimension in the East-West direction is rather small ($\sim 1'$), comparable with the dimension of the instrumental Point Spread Function: therefore, the observed spatial structure of the FilD X-ray emission is consistent with a filamentary origin. A closer inspection shows that the brightness of FilD along the North-South direction is not uniform, suggesting the presence of finer structures.

Another noticeable feature is the clump in $i0 - h0$, which is bounded by the edge of the FOV. The observed count rate here is 1.5 times the one measured in FilD, and ~ 5 times the rate in the region between Front 1 and 2.

3.2. Spectral fitting results

3.2.1. General considerations

We shall present here the spectral analysis of both RP200133 and RP500015 with an optically thin plasma emission model (Raymond & Smith 1977) and two temperature components, both in CIE conditions (hereafter called RS 2T CIE model, or simply RS 2T).

In Paper I, we performed a preliminary analysis of RP200133 with the RS 2T CIE model, and we showed that, notwithstanding the goodness of the fits, there were some topics left open. In particular, we found an apparent variation of the hydrogen column density across the image. This N_H gradient is suspicious because self-absorption should be negligible and known molecular clouds lie behind the remnant itself and hence cannot contribute to the absorption. We have now explored the possibility that this results is due instead to an intrinsic spectral variation.

To understand how this effect might occur, consider the following situation: let bin A be in CIE conditions with two component of different temperatures ($T_{A2} > T_{A1}$) and same emission measures ($EM_{A2} = EM_{A1}$), and consider an adjacent bin B having the same two temperatures (i.e. no T gradient between A and B) but $EM_{B1} < EM_{A1}$. For typical temperatures found in the Vela SNR ($T_1 = 0.1$ keV and $T_2 = 0.5$ keV, Paper I) the first component affects the PSPC spectrum mostly in the $E \lesssim 0.5$ keV, and this is also true for the interstellar absorption. Because of the limitations due to photon counting statistics and/or moderate spectral resolution, the spectral variations between bin A and B could be interpreted as a fake increase of the N_H value rather than a decrease of EM_1.

The grid layout now adopted (the same used also in Paper II) allows us to collect a number of counts per spatial bin greater than the number previously obtained with the grid adopted in Paper I, and to test in detail if the observed N_H variations are real or not. The number of counts in the spatial bins of RP200133 have been reported in Paper II and is typically about 10^4 with a maximum of 2.7×10^4. In RP500015 we have typically 2–4 $\times 10^4$ counts in each bin with a maximum of 6.5×10^4 counts. We have performed the RS 2T fits of the spectra collected in each spatial bin of the two images treating the interstellar absorption as a fixed parameter. This emission model has 4 free parameters (two temperatures and two normalization factors) and it yields 24 degrees of freedom (PSPC SASS channels 3–30 are used, corresponding to the 0.2–2.0 keV energy range). We have fixed

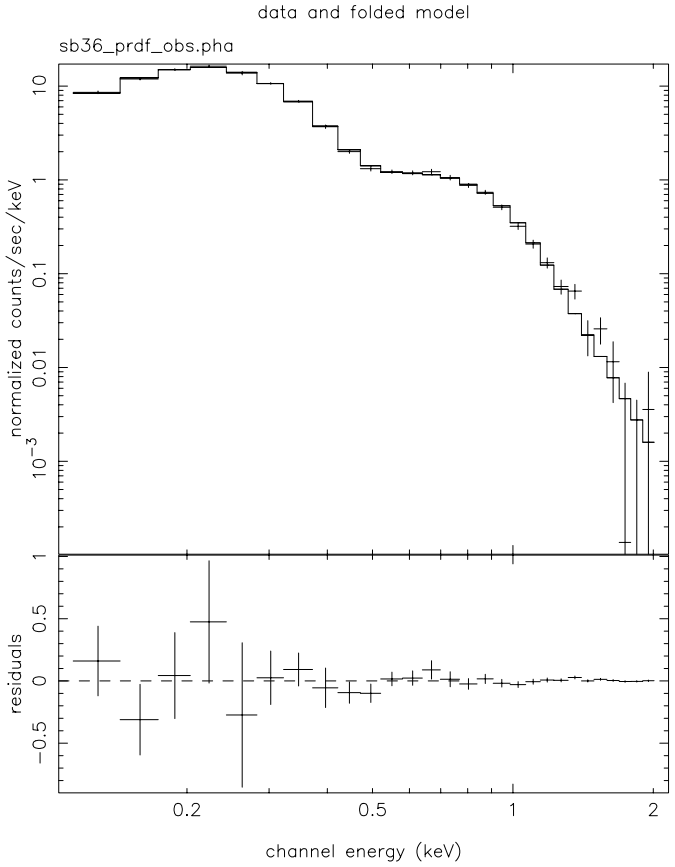

Fig. 3. The PSPC spectrum of the spatial bin $l3$ with its best-fit two-temperature CIE model.

N_H to 1×10^{20} cm^{-2} for both data sets, which is a value compatible with the measurement reported in Paper I and in Paper II, and it is also in agreement with the previous estimates of Kahn et al. (1985). In Fig. 3, we show, as an example, the PSPC spectrum of the spatial bin $l3$ ($\sim 3.5 \times 10^4$ counts) which contains the "Filament D" feature, and its best-fit 2T CIE model.

We stress that, by removing the interstellar absorption from the list of free fit parameters, the total number of free parameters is equal to the number of free parameters of the STNEI model used in Paper II. From a statistical point of view, this implies that the results here obtained with the fixed N_H RS 2T model and those obtained with the STNEI model in Paper II can be directly compared in terms of χ^2 goodness of the fit.

In the following, we use the symbol F to indicate the normalization factor $n^2V/4\pi d^2$ (which is usually given by the fit) and EM to indicate the emission measure n^2V.

3.2.2. Plasma temperatures and emission measures

In Table 2 we report the success rates of the fitting with the RS 2T CIE model in the 48 spatial bins of RP200133 and in the 56 spatial bins of RP500015, along with those results obtained in Paper II for RP200133 using the STNEI model and the ones obtained in Paper I with the RS 1T model. The table shows also the STNEI and RS 1T success rates for RP500015. The

Table 2. Fitting success rates of RP200133 and RP500015 with various emission models

Model	RP200133 Bin OK (%)	RP500015 Bin OK (%)[a]
RS 1T CIE	8 (17%)	7 (12%)
1T STNEI	21 (44%)	13 (23%)
RS 2T CIE[b]	47 (98%)	49 (88%)

[a] The number of bin with acceptable χ^2 and the corresponding percentage.

[b] For these fits, N_H was fixed to 10^{20} cm^{-2}.

4-parameter RS 2T model provides an acceptable χ^2 in most of the spatial bins (98% in RP200133 and 88% in RP500015)[2]. This result implies that data are consistent with a single N_H absorption value across the two images.

In Fig. 4, we report for both datasets the T_1 and T_2 radial profiles along each sector of the spatial grid shown in Fig. 2. The distance from the center of the remnant is reported in abscissa. For T_1, we report the profiles for each sector, whereas for T_2, given its larger uncertainties, we report a profile which is an averaged over all sectors, together with a plot of the expected Sedov profile derived following Landau & Lifshitz (1974). There are significant variations up to a factor of 2 between the best-fit T_1 temperatures measured in the same ring but in different sectors (e.g. $T_1 = 0.13$ keV and 0.08 keV in RP200133 ring 5 at ~ 18 pc) and in different rings of the same sector ($T_1 = 0.16$ and 0.11 in RP200133 ring 4 and 5 at 17–18 pc, sector b). On the other hand, from Fig. 4, it is evident that the value $T_2 = 0.5$ is statistically consistent with values measured in all the spatial bins. Moreover, the ratio of the emission measures spans a range of about two orders of magnitude ($10^{-2} < EM_2/EM_1 < 1$) and this characteristic accounts for most of the observed spectral shapes.

Fig. 5, which reports the T and EM_1/EM_2 histogram distributions, shows the clear separation between the high and low temperature component.

3.2.3. X-ray emission characteristic of Filament D

The X-ray clump named Filament D (FilD) is very peculiar, because it is isolated and it has a filamentary nature. We have performed a spectral analysis of the FilD using an extraction region with a shape matching its morphology. For this analysis, we have collected the background spectrum in a region classified as "diffuse emission" (according to Sect. 3.1) adjacent to FilD. In this way, we aim to study the peculiar characteristics of the plasma in the filament. The background subtracted spectrum has a good counting statistics (~ 9000 counts). In Table 3, we report the fitting results for FilD. Both the 1T STNEI and the 2T RS CIE model fits are acceptable. In particular, the NEI fit yields a reasonable value of the ionization time ($\tau > 300$ yr cm^{-3}), while

[2] The threshold acceptance is defined at the 95% level with 24 degrees of freedom.

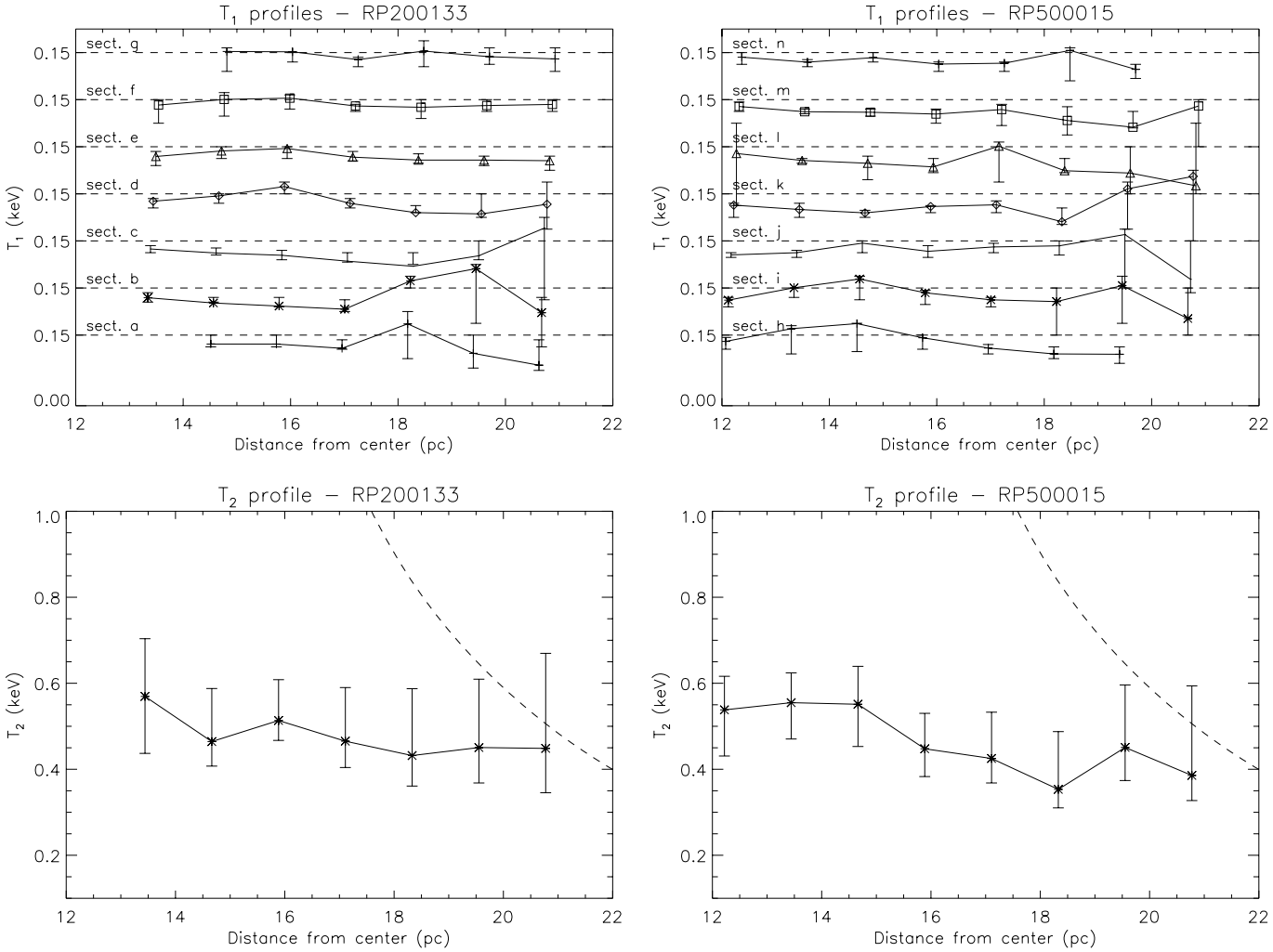

Fig. 4. T_1 and T_2 profiles for the two PSPC observations. We have excluded bins $a1$, $g1$, $h7$ and $n7$ because they contain less than 1000 counts. For T_1, we report the profiles for each sector, while for T_2 the profiles are the average of the measurements in all the sectors. We also report in the T_2 plots, the expected auto-similar Sedov profiles computed assuming typical characteristic parameters of the Vela SNR.

the 2T fit yields a best-fit emission measure ratio (EM_2/EM_1) significantly lower than the one measured in the other spatial bins. This result is due to our choice of subtracting the diffuse emission from the FilD spectrum, and indicates that there is relatively more cool plasma in the filament with respect to the surrounding regions. The $EM_2 = 0$ case (corresponding to 1T RS CIE fit) is also in the allowed emission measure range. The difference between the T_1 value in the 2T RS fit and the (higher) value in the 1T NEI fit is a measure of the error associated to the use of a CIE model instead of the NEI one. The fitting results of the whole bin $l3$ with the 2T STNEI model is also reported in Table 3, and described in the following section.

3.2.4. NEI effects

In Paper II, we stressed that a description of the Vela SNR X-ray emission in terms of a NEI emission model is necessary for a determination of the temperature and density in the shell. We showed the expected ionization time (τ) of the plasma in the shell is in the range 10^3–10^4 yr cm^{-3}, i.e. far from the equilibrium condition ($\tau > 10^5$ yr cm^{-3}). On the other hand, we have pointed out that a single-temperature description of the X-ray emission yields several interpretation problems, and that the 2T nature of the plasma is *de facto* a growing observational evidence. There is no reason to believe that the two plasma components are both in CIE conditions; instead, they may well be in NEI conditions, but, unfortunately, a spectral analysis of the Vela SNR based on a two-temperature NEI emission model is not feasible with *ROSAT* PSPC data. This is clearly shown in Table 3, in which we also report the fitting results obtained with a two-component STNEI model for the spatial bin $l3$, in which the bright clump named "FilD" is located. Notwithstanding the very high number of counts in the spectrum (2.7×10^4), the fitting parameters are unconstrained and reliable estimates of temperature and τ can not be derived, because of the moderate PSPC spectral resolution. For this reason, we adopt CIE emission models when investigating the 2T nature of the X-ray emission using *ROSAT* PSPC data.

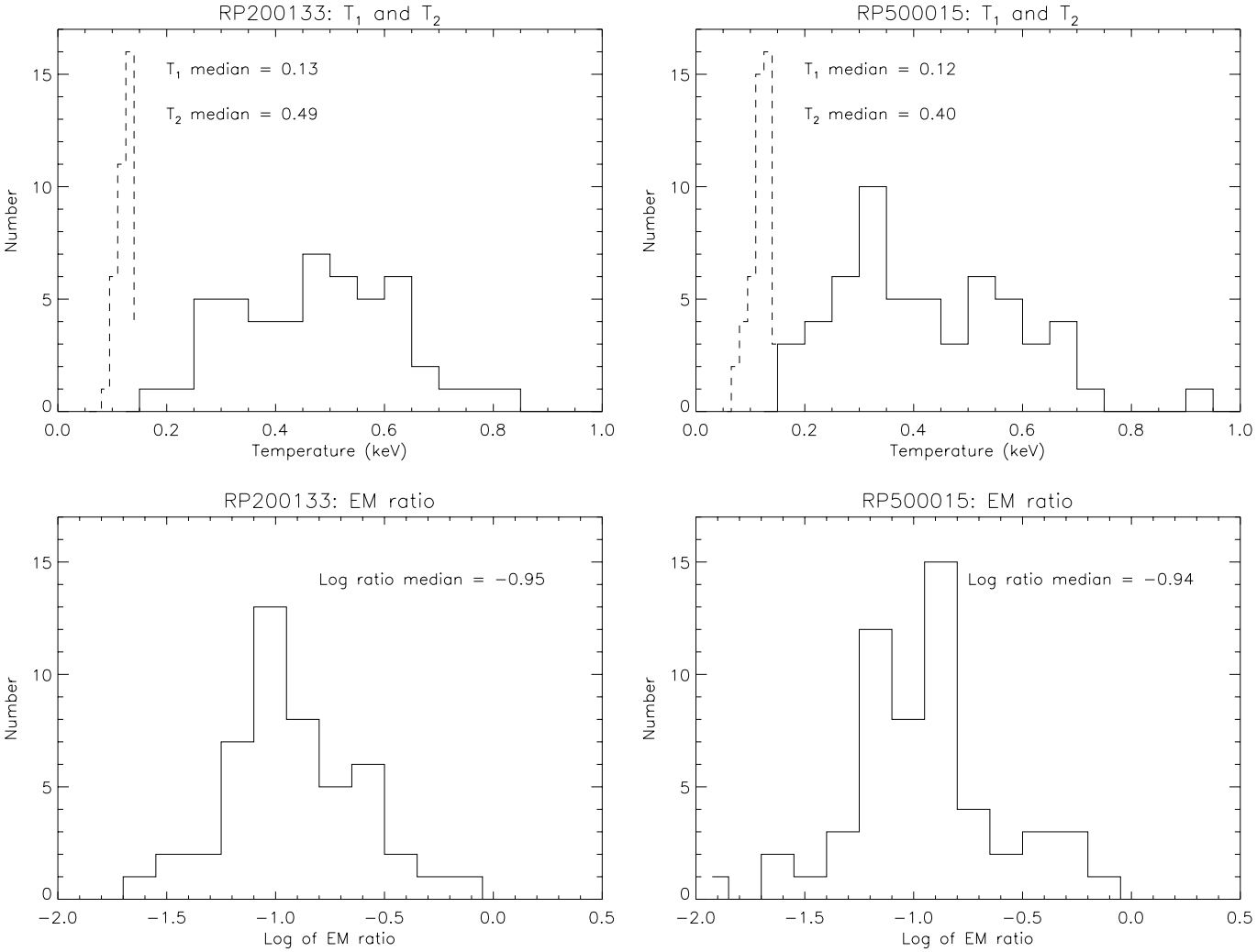

Fig. 5. T_1, T_2, and emission measure ratio histograms for RP200133 and RP500015 spatial bins. In the temperature histograms, dashed lines refer to the X1 component, solid lines to the X2 component.

To estimate the error introduced by the 2T CIE analysis of truly 2T NEI plasma, we have realized a simulation in which 200 2T STNEI spectra have been synthesized including Poisson noise, and then fitted with the RS 2T CIE model. The input parameters for the simulated spectra are: $T_1 = 0.15$, $\tau_1 = 10^4\,\mathrm{yr\,cm^{-3}}$, $T_2 = 0.5$, $\tau_2 = 3 \times 10^3\,\mathrm{yr\,cm^{-3}}$. The adopted ionization times are expected for a Vela-like SNR (Paper II): note that we have assumed $\tau_1 = 3\tau_2$ as expected in the hypothesis that the low T component originates from a plasma about a factor 3 more dense than the environment. In Fig. 6, we report the fitting results. The distributions of the best-fit temperatures and emission measures are not centered on the input values; this is particular evident for the hotter component. By computing the centroids of the distributions for the two component, we have derived that the temperatures T_1 and T_2 are underestimated by $\sim 10\%$ and $\sim 30\%$, respectively, and that the emission measures F_1 and F_2 are overestimated of $\sim 30\%$ and $\sim 90\%$, respectively.

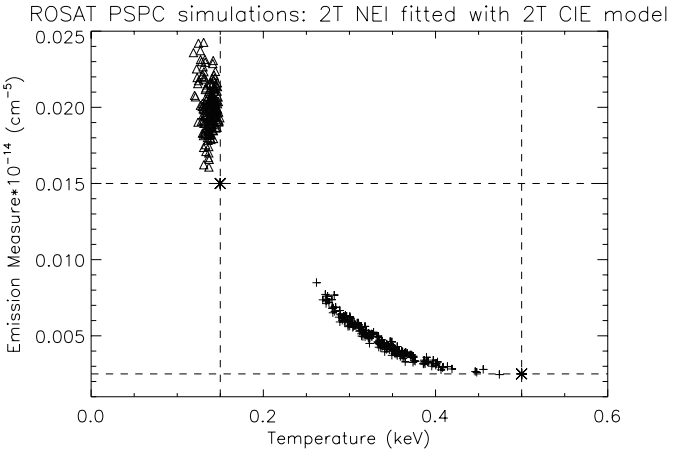

Fig. 6. Results of fitting synthesized 2T STNEI spectra with $\sim 2 \times 10^4$ PSPC counts using the 2T RS CIE model. Triangles and crosses represent the X1 and X2 component, respectively. Asterisks at the intersection of the dashed lines mark input values, which are not recovered correctly in any case.

Table 3. Best-fit parameters and derived quantities for the FilD regions

Name	T_1 (keV)	T_2 (keV)	$\log \tau$ (yr cm^{-3})	$\log F$ (cm^{-5})	n^a (cm^{-3})	χ^2/dof
1T STNEI	0.12 ± 0.03	–	> 2.5	$11.4^{+0.4}_{-0.1}$	$0.6^{+0.3}_{-0.1}$	33/24
2T RS CIE	0.095 ± 0.005	$0.5^{+0.5}_{-0.3}$	–	11.80 ± 0.02^b	0.88 ± 0.02	23/24
2T STNEI[c]	$0.12^{+0.01}_{-0.08}$	$0.8^{+\infty}_{-\infty}$	$2.6^{+1.7d}_{-\infty}$	12.2^e	1.4	15/22

[a] The density was computed using Eq. 4 in Paper I and assuming a line of sight l of ~ 1 pc, corresponding to a depth approximately equal to the N-S extension of the FilD X-ray emission. The reported uncertainty is due only to the uncertainty on F (N also scales as $\sqrt{l}$).

[b] The best-fit F_2 is $\sim F_1/130$, with $F_2 = 0$ in the acceptability range.

[c] These results were derived from a fit to a spectrum collected in bin $l3$, which includes FilD and part of its diffuse emission environment, in order to increase the total number of counts in the spectrum.

[d] The reported value is $\log \tau_1$. $\log \tau_2$ is $3.2^{+\infty}_{-0.1}$.

[e] $F_2 \sim F_1/50$.

A "zero order" correction for NEI effect can be defined from these results: in fact, in order to recover the correct values of the input 2T NEI model, the best-fit parameters should be multiplied by the following factors: $\Gamma_{T1} = 1.1$, $\Gamma_{T2} = 1.3$, $\Gamma_{F1} = 0.9$, and $\Gamma_{F2} = 0.5$. We stress that the NEI correction factor are based on a simulation with realistic but arbitrarily chosen input parameters, and that they cannot substitute a full NEI analysis which will be possible only with X-ray instrumentation with spectral resolution higher than the *ROSAT* PSPC.

4. Discussion

In Paper I, the results of the RS 2T model fitting were taken as a suggestion of NEI conditions of the emitting plasma. However, the attempt to fit the Vela SNR X-ray emission with a 1T STNEI model, carried out in Paper II yielded very low ionization times (< 10 yr cm^{-3}), difficult to support on physical grounds, and lead us to reconsider the 2T results in terms of ISM inhomogeneities. Similar results were obtained by studying the Vela SNR X-ray emission in the RP500015 image (Bocchino 1997), which is located in the same rim region of the RP200133 image, but slightly offset, thus allowing a better shell coverage.

In fact, the environment of the Vela SNR is expected to be inhomogeneous, because the wide field X-ray observations carried out using *Einstein* (Seward 1990) and *ROSAT* (Aschenbach 1993) show a patchy morphology, even though it is difficult to estimate quantitatively the size and density of the clumps embedded in it.

The observed spectrum originating from such environment comprises in general several components, whose contributions sum up along the line of sight because the plasma is optically thin. In particular, we expect contributions from: 1) plasma compressed in a thin shell just behind the shock front and likely to be out of ionization equilibrium conditions; 2) plasma in local ISM condensations (including material stripped from clouds by thermal evaporation); 3) lower density plasma in interior regions. Given the lower density of interior SNR regions predicted by the adiabatic expansion model, the latter contribution is expected to be negligible especially in the outer rings of our observations (see Sect. 4.1).

Table 4. Scheme of ISM expected phases according to the theoretical model of McKee & Ostriker (1977) and following updates.

Phase	Density cm^{-3}	Pre-shock Temperature (K)	Filling Factor
I. molecular clouds	10^2–10^3	10	0.5
II. neutral and dense clouds	$10^{1.6}$	10^2	0.02–0.04
III. corona	10^0	$\sim 8 \times 10^3$	0.2
IV. low density	$10^{-2.5}$	$10^{5.7}$	$< 0.2^a$

[a] McKee & Ostriker (1977) reported a filling factor value of 0.7–0.8 for this phase because they did not consider phase I.

In this perspective, it is possible to interpret the two-component nature of the Vela SNR X-ray spectrum as a tracer of the presence of two phases in the ISM swept up by the shock. This interpretation, which has not been often investigated in the literature, could hold even for other middle-aged SNR, since they are expected to interact with inhomogeneous environments (for instance, for the Cygnus Loop see Decourchelle et al. 1997); successful fitting results with 2T models have been reported in the cases of IC443 (Asaoka & Aschenbach 1994), SN1006 (Willingale et al. 1996), G296.1-0.7 (Hwang & Markert 1994) and RX04591+5147 (Yamauchi et al. 1993) but the physical interpretation in terms of ISM inhomogeneities, as the one we propose, has not been investigated.

In this section, we shall follow the hypothesis of an association of the two X-ray emission components (X1 corresponding to the cooler component, and X2 to the hotter component) with two ISM phases having different densities. This association will allow us to estimate the SNR explosion energy and distance by applying the Sedov analysis to the X-ray component likely associated with the inter-cloud ISM phase. The results we obtain in this way are more accurate than those previously derived by spectral analysis based on single-temperature models.

4.1. Interpretation of the temperature components

In Table 4, we list the expected ISM phases together with their respective values of temperature, T, density, n and filling factor,

f. The table is based on the work of McKee & Ostriker (1977) and subsequent revisions (Slavin & Cox 1993, Cox 1993, Shelton & Cox 1994). The presence of the low density phase IV is in doubt (Korpela et al. 1998), while the presence of molecular clouds is well established.

The ISM model reported in Table 4 is our starting point for the interpretation of the two components detected in the X-ray emission of the Vela SNR rim. Let us consider a middle-aged SNR shock wave, which propagates in a ISM as described in Table 4, and let us assume that the shock velocity v_s is $\sim$ 200–600 km s^{-1} when the shock front is in phase III. The post-shock temperature will be in the range 1–5 $\times 10^6$ K, and hence the plasma will emit in the X-ray band. As the shock encounters an inhomogeneity, it enters phase II which is ~ 40 times denser than phase III. The secondary shock transmitted in phase II is ~ 6 times slower ($\rho_{II} v_{II}^2 = \rho_{III} v_{III}^2$ according to McKee & Cowie 1975), thus heating the shocked material at a temperature 40 times lower, and driving the bulk of the emission outside the X-ray band. For the same reason, the shocks propagating in the phase I medium will achieve even lower temperatures.

Although, to be more realistic, continuous distributions of density should replace the "step variations" of Table 4, this simple scheme suggests that the temperature of the shocked plasma is somewhat determined by the density of the layers which the shock encounters during its propagation. From this point of view, we expect that X-ray observations probe the hotter and less dense plasma in the external regions of ISM inhomogeneities and the inter-cloud medium, while UV and optical observations trace cooler and more dense regions, associated with clouds internal layers. What it is still to be assessed now is a possible correspondence between the two X-ray emission components and some of the ISM phases described above. Our working hypothesis is that the hotter X-ray component (X2) is mainly associated with the "inter-cloud" plasma in which adiabatic expansion of the main shock occurs, while the cooler component (X1) originates from local ISM "inhomogeneities".

Our interpretation of the hotter X-ray component is not in contrast with the observed flat temperature profiles shown in Fig. 4, significantly different from the steep profile predicted by the Sedov model. This is because the X-ray emission we observe at any location of the spatial grid mainly originates from a thin layer behind the shock front, where the plasma density and hence the emission measure are the highest. The more internal (and hotter) spherical shell layers have much lower densities and do not contribute appreciably to the total X-ray emission. In fact, assuming a Sedov profile for the temperature and density of the plasma, we have estimated that more than 80% of the total emission is generated within a shell thickness $\sim$ 8% of the remnant radius, i.e. within ~ 2 pc in the case of the Vela SNR. Hence, in X-rays we see the external layer whichever direction we point at, measuring the same average temperature.

Finally, the fact that T_1 cannot be considered uniform while T_2 can be, is in agreement with our hypothesis, since the putative ISM clumps which give rise to the X1 component could have in principle very different densities, yielding different X-ray temperatures.

In the following, we will use the terminology "inter-cloud component" and "inhomogeneities component" with reference to the hotter and cooler X-ray component, respectively.

4.2. Densities and filling factors of the post-shock plasma components

We now use the fitting results to derive the plasma density and filling factor of each component. These quantities are useful to understand the relation between the X-ray morphology (in particular, the X-ray clumps as defined in Sect. 3.1) and the ISM phases. While the X-ray clumps are generally interpreted as tracers of ISM cloud, it is not clear how they are formed. In particular, there are at least 3 possible scenarios: clouds evaporation, bow shock, or secondary shock compression inside the cloud. In order to test these alternatives, an estimate of the density and filling factor is required.

Let $V = Al$ be the volume of emitting plasma from which the emission we observe in a given spatial bin of our image originates. Here, A is the area subtended by the $10' \times 10'$ spatial bin, and l is the line of sight segment enclosed in the spherical SNR shell. The validity of the RS 2T model in a large fraction of the bins suggests that the two components are present in the volume V at the same time. We can therefore define a volume filling factor for each component in each spatial bin (f_1 and f_2 for the component X1 and X2, respectively), analogous to the filling factor used in Table 4. The brightness of a given component is proportional to f and to the square of the density through the normalization factor (derived from the spectral fit):

$$F_i = \frac{n_i^2 V_i}{4\pi d^2} = \frac{n_i^2 f_i V}{4\pi d^2} \tag{1}$$

where n_i and V_i are the density and volume of the plasma associated to the i-th emission component, and V is the total volume. Hence, the ratio of the normalization factors of the two components can be written as:

$$\frac{F_2}{F_1} = \frac{n_2^2 f_2 V}{n_1^2 f_1 V} = \frac{n_2^2 (1 - f_1)}{n_1^2 f_1}. \tag{2}$$

It is clear that the filling factor estimate has a twofold importance: first, it allows us a direct comparison with the theoretical expectation summarized in Table 4; second, it can be used in Eq. 1 to derive the density.

The calculation of f_1 for each spatial bin requires an independent estimate of the density ratio, and this can be obtained with the following reasoning, in the framework of our working hypothesis. If the X1 component is due to a strong bow or secondary shock propagating inside an ISM cloud, then we can use the results of McKee & Cowie (1975), which have shown that $\rho_1 v_1^2 = \rho_2 v_2^2$, where the subscripts refer to the two components. Since the square of the shock speed is proportional of the temperature behind the shock, we have

$$\frac{n_2}{n_1} = \frac{v_1^2}{v_2^2} = \frac{T_1}{T_2} \tag{3}$$

If instead the X1 component is due to material evaporated from ISM clouds, then we have $\rho_1 v_1^2 \geq \rho_2 v_2^2$, where the equal sign

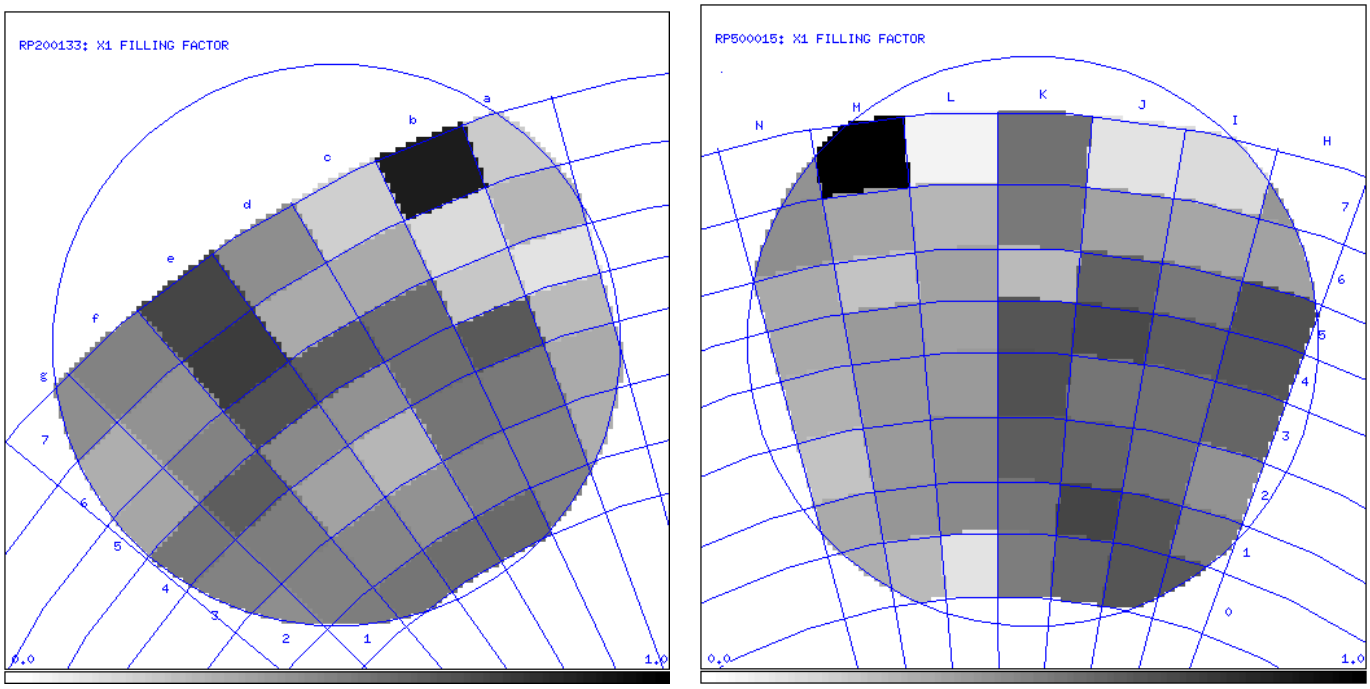

Fig. 7. Map of the filling factor of the X1 component in the image of RP200133 (*left panel*) and RP500015 (*right panel*).

holds only if the evaporation is not violent, and hence quasi-isobaric. As we shall see in the following section, the physical conditions behind the Vela SNR shock are such that the evaporation parameter is well below unity, indicating that the evaporation, if present, is far from being saturated, and therefore is unlikely that we have strong pressure gradients. Under these circumstances, the relation $\frac{n_2}{n_1} = \frac{T_1}{T_2}$ may be valid in both the evaporation and strong shock scenario.

Using Eq. 3 and Eq. 2 we can derive the filling factor,

$$f_1 = \left(\frac{F_2}{F_1} \frac{T_2^2}{T_1^2} + 1 \right)^{-1}. \quad (4)$$

In this equation, f_1 is a function only of the best-fit quantities. We note that, even in the unlikely case of violent evaporation as discussed above, Eq. 4 provides us with an upper limit on the filling factor. In Fig. 7, we show a map of the parameter f_1 in each of the two images we are considering. The filling factor is always in the range 0.2–0.8: high f_1 values (> 0.5) are often associated with X-ray bright "clumps", as defined in Sect. 3.1, especially in RP200133; instead, in RP500015, sectors l, m, and n inside ring 4 have high brightness and $f_1 < 0.5$, so that high surface brightness does not necessarily imply high f_1 values.

We stress that the filling factors reported in Fig. 7 were derived in the hypothesis that there are only two thermal components emitting in the volume V (i.e. $f_1 + f_2 = 1$). In the case that an additional component is present, f_1 should be corrected by a factor $1 - f_3$, where f_3 is the volume filling factor of the third component. Detailed photometry and spectrophotometry of this region of the Vela SNR shell, which will be fully presented in a forthcoming paper, shows that a third component is actually present and it is responsible of the optical emission of filaments. Hester (1987) has shown that optical filaments arise from thin sheets of compressed material; if the width of the sheet is $< 10^{17}$ cm (Hester 1987 took 10^{16} cm), then the volume filling factor of the filaments in one of our spatial bin is < 0.08. Therefore the filaments occupy a small fraction of the volume and $f_1 + f_2 = 1$ is a good approximation.

Now, from the value of f_1, we can derive the density in each spatial bin. Since $V = Al$ and $A = \Theta d^2$, where Θ is the solid angle subtended by each spatial bin in Fig. 2, and d is the distance of the Vela SNR, we can rewrite Eq. 1 in the following way:

$$F_i = \frac{n_i^2 f_i \Theta l}{4\pi}. \quad (5)$$

The densities are therefore given by:

$$n_1 = \sqrt{\frac{4\pi F_1}{f \Theta l}} \quad (6)$$

$$n_2 = \sqrt{\frac{4\pi F_2}{(1-f)\Theta l}} \quad (7)$$

with a typical error of ± 0.1 on n_1 and ± 0.2 on n_2, derived from the statistical uncertainties of F_i. The dependence of the density on the the line of sight is not strong, and we have estimated l assuming that the emitting plasma is confined in a spherical shell of thickness 2 pc.

The possible presence of NEI effects, already addressed in Sect. 3.2.4, may introduce a further bias in the evaluation of the filling factor or density, as we have seen in Sect. 3.2.4 for T and EM. Following the same reasoning, we have evaluated the bias which would be introduced by our CIE spectral analysis if the plasma was effectively in NEI conditions. We have computed

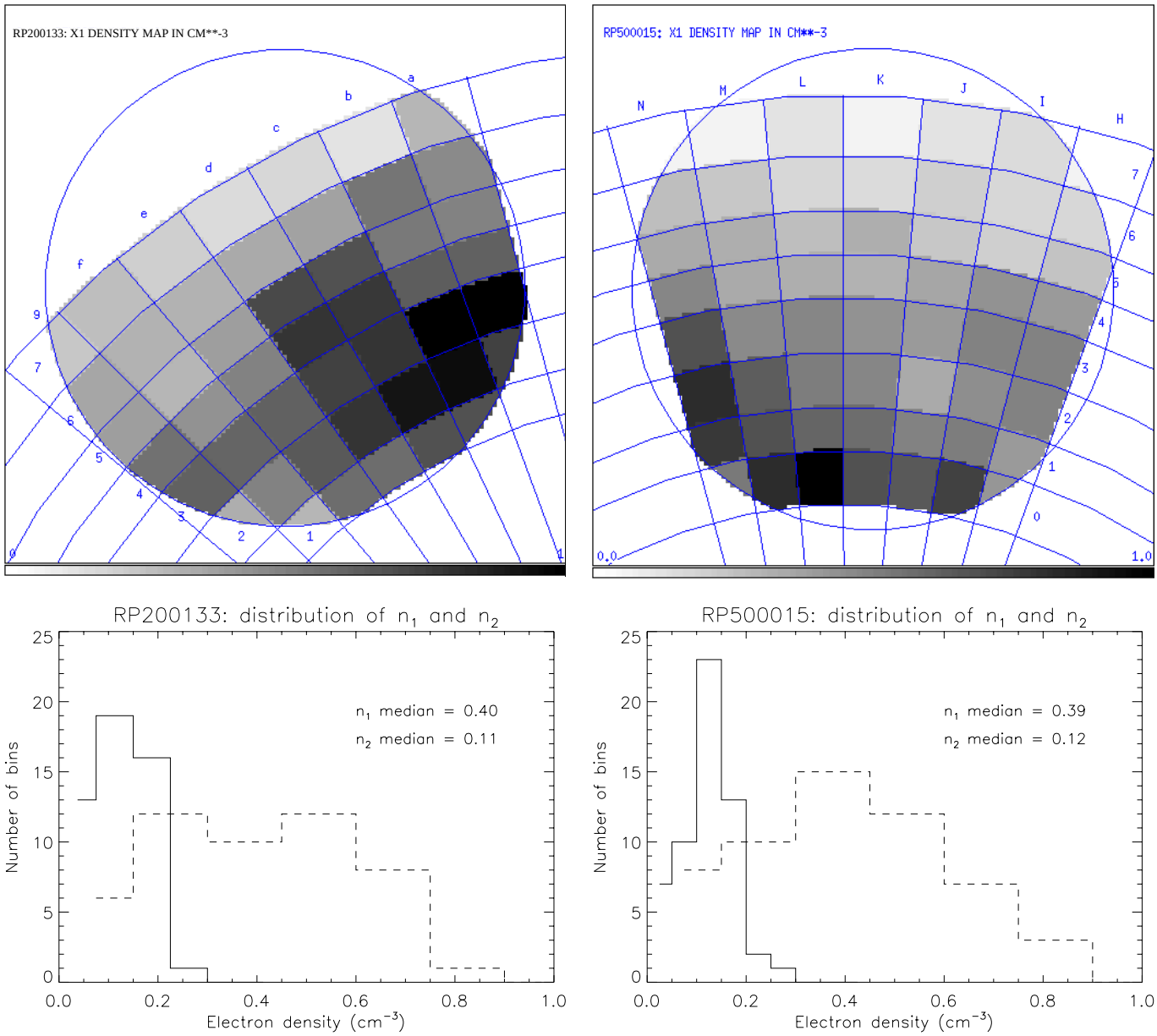

Fig. 8. Map of the density of the X1 component (n_1, *upper panels*) and histograms of n_1 and n_2 (*lower panels*). The data for RP200133 are on the left, whereas the data for RP500015 are on the right.

f_1 and n according to Eqs. 4 and 7 using the input and simulated values for F and T, deriving an "input" $f-1$ and n and their corresponding values derived from CIE fittings. We derived that the correction factor for f_1 (Γ_{f_1}) is 0.84, for n_1 (Γ_{n_1}) is 0.96, and for n_2 (Γ_{n_2}) is 0.79, which are near to unity, especially for n_1.

In Fig. 8, we show the n_1 density map in each field of view, along with the histograms of n_1 and n_2. The cooler X1 component density is on average a factor of 3 higher than the hotter X2 component density. The figure also shows that higher n_1 regions in RP200133 correspond in most cases to the brightness-defined "clumps" (Sect. 3.1, zone A and B in Paper I). Therefore, in these regions, the high brightness is due to high filling factors and also to high densities ($n_1 = 0.8$–$1.0\,\mathrm{cm}^{-3}$ in $d5$, $c4$, and $b3$, whereas $n_1 = 0.5$–$0.7\,\mathrm{cm}^{-3}$ in surrounding regions, such as $e4-e5$, $b5$ and $c1-d1$). In RP500015, the luminosity "clumps" in sectors m and n also correspond to high density values ($n_1 > 0.7\,\mathrm{cm}^{-3}$), but many of the "clumps" have low densities ($n \lesssim 0.5\,\mathrm{cm}^{-3}$). Therefore, in the case of RP500015, some of the brightness enhancements seem to be generated only by an increase of the filling factor of the inhomogeneities.

Since $f_1 \geq 0.2$ in all the spatial bins of both sequences, there is always a sizable fraction of volume occupied by the cooler gas associated to the inhomogeneities. This means that the ISM inhomogeneities affect not only the regions classified as "clumps", but also most of "diffuse emission" of the Vela shell, at least in the 7–8 pc covered by the two adjacent images. In particular, the determination of f and n allows us to better

characterize the nature of inhomogeneities in some case. For instance, in the spatial bin $l3$ of RP500015 which contains FilD we have $f_1 = 0.4$ and $n_1 = 0.5$, while in the "Front 1" region of the same image (bins $k1 - h1$ and $k0 - h0$) the density is comparable with FilD, but the filling factor is sensibly higher. This suggests that FilD is probably an isolated cloud with a small extension along the line of sight and that Front 1 is a set of several clouds or a cavity wall with a greater extension along l. This is in agreement with the fact that the spectral analysis of the very bright region including FilD of Sect. 3.2.4, which is sensibly smaller than the spatial bin $l3$, gave a density of $0.88\,\mathrm{cm}^{-3}$ (Table 3) greater than the average $l3$ density.

4.3. Clouds evaporation

The evaporative cloud scenario has been proposed by McKee & Cowie (1975) and discussed in the framework of SNRs by Charles et al. (1985), Ku et al. (1984), White & Long (1991), Dalton & Balbus (1993), and Bandiera & Chen (1994). Comparisons with observed SNRs, carried on, for instance, by Harrus et al. (1997) on W44, Craig et al. (1997) on CTB1, Fuerst et al. (1997) on G18.95-1.1, have shown that thermal evaporation is generally consistent with the radial profiles of plerionic and composite SNRs, but not with shell SNRs.

In this section, we will check if cloud evaporation is consistent with our data. To do that, we estimate the plasma density of the X1 component and we check if the evaporation efficiency is high enough to create the observed quantity of cool plasma.

For a given spatial bin, the total emitting mass of the X1 component is given by

$$m_1 = n_1 V_1 m_p = \frac{4\pi d^2 F_1}{n_1} m_p \tag{8}$$

which is derived by inverting Eq. 1. For instance, we typically have $F_1 = 2 \times 10^{12}\,\mathrm{cm}^{-5}$, and $n_1 = 0.5\,\mathrm{cm}^{-2}$, yielding $m_1 = 3$–9×10^{31} g for a distance between 200 and 350 pc. The evaporated mass in a time interval t from a cloud is given by $m_{evap} = \dot{m}t/m_p$, where m_p is the proton mass. An analytical expression for $\dot{m}$ has been derived by Cowie & McKee (1977) under classical and saturated conduction. In our case, the dimensionless saturation parameter is very low ($\sigma_0 \propto T_{ic}^2/nr_c$ is 0.1 using our best-fit T_2 as inter-cloud medium temperature, n_2 as medium density and $r_c = 2\,\mathrm{pc}$, in Eq. 32 of Cowie & McKee 1977), and the classical conduction formula applies:

$$\dot{m} = 2.75 \times 10^4 T_{ic}^{5/2} r_c \frac{30}{ln\Lambda}\ g\ s^{-1} \tag{9}$$

where r_c is the cloud radius in pc, T_{ic} ($= T_2$) is the inter-cloud medium temperature, and assuming negligible magnetic fields. Using $r_c = 2\,\mathrm{pc}$, estimated from the size of the clumps in the X-ray image, and $T_{ic} = 5.2 \times 10^6\,\mathrm{K}$ (as derived from the X2 component), we obtain $\dot{m} = 1.6 \times 10^{21}\,\mathrm{g\,s}^{-1}$, and therefore one cloud would take 600–2000 yr to accumulate the observed mass. Since we expect that the shock travels 1 pc (the effective spatial resolution of our grid) in $\sim 2 \times 10^3$ yr, we conclude that our results are consistent with the evaporative model.

Inhomogeneities with radii smaller than 2 pc have lower evaporative loss rates but can be present in larger number, and therefore cannot be excluded. Larger clouds in principle yield enough mass, but their presence would have dramatic effects on the SNR dynamics, yielding clearly visible variations of the X-ray brightness over spatial scales larger than $\sim 20'$. This may be the case of the feature identified as Front 1 in RP500015, which extends over 4 pc or more.

4.4. The distance and explosion energy of the Vela SNR

We now apply the Sedov analysis to the X2 component, which we have associated to the main blast wave expanding in the inter-cloud medium, in order to derive the remnant characteristic parameters (e.g. the distance and the explosion energy).

The cloud filling factor is $\gtrsim 0.5$ in about 60% of the bins. The main shock front is certainly distorted by the impact with the clouds, but several hydrodynamical simulations show that the distortions tend to disappear after the shock has overrun the cloud (Bedogni & Woodward 1990). Moreover, Cowie et al. (1981) have verified that clouds with 5 pc radius and inter-cloud density $0.3\,\mathrm{cm}^{-3}$ do not affect the whole expansion dynamics of the SNR and hence the average temperature profile. This conclusion certainly applies to our case, since the inhomogeneities we observe have sizes < 5 pc. It is therefore possible to apply the Sedov analysis to the inter-cloud component we have isolated in the X-ray emission. In practice, we have estimated n_2 according to Eq. 7, the pressure according to the relation $p = 2nkT$, and the velocity from the relation $T \propto v_s^2$. These quantities, derived from the X2 component, represent post-shock values. We adopted as our best estimate for a given observation, the average of each quantity across the whole set of bins in which the 2T model provides a statistically acceptable description of the spectral data. Moreover, since the values derived from RP200133 and RP500015 are compatible within the uncertainties, and the two sets of measurements are independent from each other, we adopted as our best estimates for both regions the mean of the average values. Summarizing the results and related uncertainties:

1. the electron temperature behind the shock is 5.2 (3.5–7.5) $\times 10^6$ K;
2. the ion density behind the shock is 0.11 (0.05–0.2) cm^{-3}. For an adiabatic shock, this means that the ISM density is 0.03 (0.01–0.05) cm^{-3};
3. the pressure behind the shock is $\sim 6 \times 10^{-10}$ dyne cm^{-2} which is reasonable for a typical Vela-like SNR (see, for instance, Cui & Cox 1992);
4. the shock speed is 600 (500–730) $\mathrm{km\,s}^{-1}$, assuming equal electron and ion temperatures behind the shock. This is also a plausible shock speed for a Sedov SNR with the age of the Vela SNR.

To derive the explosion energy and the SNR radius, we apply the Sedov analysis using the above shock speed and density, and the SNR age derived by the PSR0833-45 characteristic age. The connection between the pulsar and the SNR is rather es-

tablished (Weiler & Panagia 1980, Weiler & Sramek 1988) and its age has been accurately assessed ($P/2\dot{P} \sim 11200$ yr, Taylor et al. 1993). The Sedov analysis yields an explosion energy of $1.2^{+4.1}_{-1.0} \times 10^{50}$ erg, a value lower than the canonical one quoted for supernova explosions ($\sim 10^{51}$ erg), but not unreasonably low. In fact, Nomoto et al. (1976) showed that the expected explosion energy could be as low as 5×10^{49} erg, and Aschenbach et al. (1991) derived 5×10^{49} erg for G18.95-1.1 on the basis of a similar Sedov analysis applied to a ROSAT All-Sky Survey observation. Another low value (2–30×10^{49} erg) was derived by Hughes & Singh (1994) for the SNR G292.0+1.8. Our derived energy is lower than previous estimates for the Vela SNR: for instance, Gorenstein et al. (1974) derived $E > 4 \times 10^{50}$ erg using a 1T model and low spatial resolution data. Our results should be more reliable since they are based on a more accurate model of the post-shock regions and on data with better spatial resolution. More recently, Jenkins & Wallerstein (1995) derived $E = 1$–2×10^{51} erg assuming a SNR distance of 250 pc, and a ram pressure of 2–4×10^{-9} dyn cm^{-2}; their estimate is based on absorption measurements along the line of sight in a region on the West part of the shell, very far from our pointings, and their value could be affected by the local physical conditions. Our estimate, instead, is an average on a large sky area of the X2 component and it is less (in principle not at all) affected by the clumpy environment of the Vela SNR.

Using the Sedov relations, as given for instance, by McKee & Hollenbach (1980), we derive the real SNR radius, which turns out to be 17^{+26}_{-10} pc. The apparent radius in the sky of the Vela shell has been recently measured on the basis of *ROSAT* All-Sky Survey observations by Aschenbach (1993), and it is of 3.6°. We therefore derive a SNR best-estimate distance of 280 pc, and in any case in the range between 110 and 680 pc. Our derived best-estimate value is lower than the often quoted value of 500 pc based on the old estimate of Milne (1968), even if it is not incompatible considering the allowed range. A critical review of the Milne results made by Oberlack et al. (1994) has shown that Milne made a wrong assumption of the real shell radius, and that a new computation of the distance based on the Milne data is 230 pc, which is in good agreement with our best-estimate value. Oberlack et al. (1994) also stressed that independent preliminary results based on *ROSAT* data indicate a distance < 350 pc.

We have evaluated the influence of the NEI effects on the Vela SNR characteristic parameters, as outlined for T and EM in Sect. 3.2.4. The corresponding correction factors are: $\Gamma_{E_{51}} = 1.5$, $\Gamma_{r_{sh}} = 1.16$ and $\Gamma_d = 1.12$. The parameters values corrected for the NEI effects are: $E_0 = 1.8^{+6.2}_{-1.5} \times 10^{50}$ erg, $r_{sh} = 20^{+29}_{-12}$ pc and $d = 315^{+470}_{-190}$ pc. The differences between these values and the ones derived assuming CIE conditions do not change our conclusions.

4.5. Energy equipartition between electrons and ions

Many of the considerations we have done are based on the hypothesis of instantaneous electron-ion energy equipartition. In fact, it is well known that the temperature derived by the X-ray spectral analysis is the electron temperature T_e, and to derive the shock velocity applying the Sedov analysis we need the ion temperature T_i. The equipartition therefore plays a crucial role in the study of SNRs and it is still the subject of many debates (Masai 1994, Laming et al. 1996). In particular, it is classically expected that $T_e = \frac{m_e T_i}{m_p}$ just behind a strong shock and that the equipartition time is longer than the age of the oldest SNRs (Spitzer 1962). Since the SNR shell strongly emits thermal X-ray radiation even in the vicinity of the putative position of the blast wave, the classical theory should be reviewed and mechanisms based on plasma instabilities have been invoked to explain the apparent faster-than-classical equilibration (McKee 1974, Cargill & Papadopoulos 1988, Lesch 1990). On the other hand, strong observational constraints on the relation between T_e and T_i still lack. On the basis of our results, we can derive some hints on this relation in the Vela SNR shell.

According to the Sedov model which we have applied to the X2 component, we have:

$$T_{i7} = \left(\frac{0.4}{t_{10^4}}\right)^{\frac{6}{5}} \left(\frac{E_{51}}{n_0}\right)^{\frac{2}{5}} \tag{10}$$

with T_{i7} is the ion temperature in units of 10^7 K, t_{10^4} is in units of 10^4 yr, n_0 in cm^{-3} and E_{51} in 10^{51} erg. By inserting appropriate t and n_0 values, and using an upper limit for the explosion energy in units of 10^{51} erg (E_{51}), we obtain a corresponding limit on T_i. In the hypothesis of no instantaneous electron-ion energy equipartition, $T_i = kT_e$, where $1 \ll k < 1836$. For instance, if $E_{51} \lesssim 1$, which should be reasonable for typical supernova explosions (Lattimer et al. 1985), $n_0 = 0.03$ cm^{-3} and $t = 11200$ yr, we get $T_i \lesssim 1.1 \times 10^7$ K $\sim 2.1 T_e$. This means that our data are not incompatible with deviation from energy equipartition, but we exclude large deviations, such as the one expected in case of slow Coulomb collision-driven equipartition of Spitzer (1962). Moreover, we stress that if $E_{51} = 1$ and $T_i = 2.1 T_e$, the Sedov derived SNR distance would be 420 pc, which is larger than the recent constraints of the Vela SNR distance reported by Oberlack et al. (1994). If the plasma is in NEI, we have derived, following Sect. 3.2.4, that T_1 computed according to Eq. 10 should be increased by a factor 1.17. Therefore, we conclude that k should be in the range 1–2.5 with low values favored by consistency checks. Fast equipartition is also compatible with observation of some other SNRs, as reported by Laming et al. (1996) and Willingale et al. (1996).

4.6. Comparison of parameters derived with different emission models

Our determination of the remnant characteristic parameters provides us with the possibility to make a consistency check of our hypothesis about the association between the X2 component and the inter-cloud medium by comparison between the values derived from the 2T model fitting with the corresponding values derived assuming 1T models, and by the comparison with values published in literature. In Table 5 we summarize the Vela SNR parameters derived from the X2 component of our 2T model and those derived from the fitting results with the STNEI model

Table 5. Vela SNR characteristic parameters derived from Sedov analysis of X2 component of the RS 2T model and from the RS 1T model.

	RS 2T (X2)			STNEI			RS 1T		
	Min	Med	Max	Min	Med	Max	Min	Med	Max
T_i (10^6 K)	3.5	5.2	7.5	1.7	2.3	5.8	1.6	2.0	2.4
v_s (km s^{-1})	500	600	730	350	400	640	285	310	350
n_{ps} (cm^{-3})	0.05	0.11	0.2	0.07	0.17	0.28	0.1	0.15	0. 40
P (10^{-10} $\frac{dyne}{cm^{-2}}$)	2	6	12	2	6	12	0.5	0.7	2
E_0 (10^{49} erg)	2	12	53	0.4	2	38	0.3	0.6	3
r (pc)	7	17	43	4	12	44	4.5	9	20
d (pc)	110	280	680	70	185	695	70	145	300

Table 6. Comparison between X-ray derived results and ISM phases.

Name of the phase[a]	Temperature post-shock (K)	Density pre-shock (cm^{-3})	Density post-shock (cm^{-3})	Observational evidence	Association with ISM model[b]
Inter-cloud	5.2×10^6	0.03[c]	0.11	X2 (hot) component	Phase III.5
Inhomogeneities	1.3×10^6	0.13[c]	0.5	X1 component and X-ray "clumps"	Phase III (clouds' corona) or gas evaporated from Phase II (clouds)

[a] In this column we report the names introduced in Sect. 4.1.
[b] This is a temptative correspondence with the McKee & Ostriker (1977) + updates ISM model reported in Table 4.
[c] Derived from $n = n_0/4$.

of Paper II and with the 1T RS model of Paper I. We stress that, to produce Table 5, we have used only the fitting results in those spatial bins which are acceptable according to the χ^2 test (at the 95% confidence level). We note that, while the normalization factors (F) derived by different models are similar, the explosion energy values (E_0) is unreasonably low for the RS 1T model and still very low for the 1T STNEI model, confirming that the X2-intercloud association represents the most realistic description. In fact, the energy derived with the 1T RS model, is always $< 3 \times 10^{49}$ erg, i.e. below the lower limit quoted by Nomoto, Sugimoto & Neo (1976) for typical supernovae explosions, due to the low values of the plasma temperature ($E_0 \propto v_s^5 \propto T^{5/2}$ in the Sedov model), obtained because the emission measure is dominated by the inhomogeneities. Table 5 also shows that the 1T spectral analysis, which has been performed in other middle-aged SNR (for instance, on G18.95-1.1 by Aschenbach et al. 1991, and on RX04591+5147 by Pfeffermann et al. 1991) could have yielded biased results, since the 2T nature of the X-ray emission may be very common in these objects. The derived pressure, $P < 2 \times 10^{-10}$ dyn cm^{-2} also represents a problem with the 1T RS model, since, according to the results of Cui & Cox (1992), such a value is more appropriate for an age of 4×10^4 yr rather than for the estimated Vela SNR age of 1.1×10^4 yr, while the 2T model provides us with a more reasonable value.

4.7. Comparison with ISM models

Here we review our results about the nature of the sources of the Vela SNR X-ray emission and we compare them to the multiphase ISM model introduced by McKee & Ostriker (1977, hereafter MO77) and subsequently updated. We stress, however, that both the X-ray emission model and the ISM model are based on a small number of discrete components and thus is just an approximation of the more realistic smooth variations of the physical parameters between different phases.

In Table 6, we report the physical parameters of the two X-ray components and their association with ISM phases. Our best-estimate for the inter-cloud medium density is 0.03 cm^{-3}, significantly higher than the density of the phase IV reported by MO77 (0.004 cm^{-3}).

Therefore, we argue that the phase IV is incompatible with our results, in agreement with recent results which have posed strong constraints on the existence of a very low density and very hot ISM phase (Korpela et al. 1998) and the SNR ability to produce a detectable fraction of hot gas (Slavin & Cox 1993; Shelton & Cox 1994). We therefore associate the X2 component to a shock propagating in what we have called phase III.5 in Table 6, which have characteristics intermediate between the MO77 phases III and IV. In particular, the density of phase III.5 is always higher than 0.01 cm^{-3}, and its pre-shock temperature is lower than that reported by MO77 for the phase IV, in agree-

ment with the low abundance of O VI reported by Korpela et al. (1998).

The inhomogeneities associated to the X1 component, represents the boundary between the phase III.5 and the ISM clouds' corona (phase III of MO77). We note that, according to MO77, a typical ISM "cloud" has a density of $10\,\mathrm{cm}^{-3}$ or more, while the post-shock density derived by the X1 component is only $0.5\,\mathrm{cm}^{-3}$. This may somewhat favour the interpretation of the X1 component in terms of gas evaporated by dense clouds overrun by the blast wave, but on the other hand there is in principle no reason why the ISM clouds should have only densities of $10\,\mathrm{cm}^{-3}$ or higher, and hence the non-evaporative isolated cloud model is equally feasible.

The fact that we do not detect ISM inhomogeneities with density higher than 0.5–1 cm^{-3} is caused by the fact that the propagation of the Vela shock inside them would not produce detectable X-ray emission, but only UV and optical emission. It is therefore of great importance to analyze the optical emission of these rim regions, and to study the relative position of X-ray and optical filaments. This will be done in a subsequent paper, in which we shall discuss the physical characteristics of the most dense regions of the ISM inhomogeneities, as obtained from observations with IUE and from optical spectrophotometry of selected filaments with the ESO 2.2m telescope.

5. Summary and conclusions

We have applied single-temperature (1T) and two-temperature (2T) emission models to the spectral analysis of two X-ray observations of the North-East of the Vela SNR shell. Given the difficulties to explain the low ionization times derived assuming a 1T NEI model (Paper II), we have reconsidered the success of the 2T CIE model fitting as a direct evidence of ISM inhomogeneities rather than evidence of NEI, and we have associated the two components (the cooler X1 component and the hotter X2 component) to two ISM phases (an higher density "inhomogeneities" phase and a lower density "inter-cloud" phase, respectively). This association is supported by the clumpy X-ray emission morphology, as suggested for instance by Aschenbach (1993). Considering first the cooler X-ray component, we have found that:

1. the ISM is inhomogeneous in both the observed regions (RP200133 and RP500015). In any spatial bin the volume filling factor of the inhomogeneities is > 0.2, and in 60% of the spatial bins is > 0.5, i.e. the inhomogeneities are dominant in volume;
2. ISM inhomogeneities may create X-ray clumps in two ways. In one case (mostly in RP500015), several inhomogeneities with a typical density of $0.5\,\mathrm{cm}^{-3}$ overlap along the line of sight to yield a filling factor > 0.5. In other cases (mostly in RP200133 and in sectors m and n of RP500015, which are adjacent to sectors a and b of RP200133) the bright X-ray clumps are caused by a joint increase of filling factor and density of the inhomogeneities (up to $1.0\,\mathrm{cm}^{-3}$). The latter is the case of the X-ray feature "Filament D", which may be produced by an isolated ISM clouds more dense than the surroundings inhomogeneities;
3. Fig. 2 shows that the clumps have sizes of few parsecs. The rebinning scheme we have adopted, which represent the best compromise between spatial resolution and photon counting statistics, has allowed us to perform spectral analysis on scales of than $\sim 1\,\mathrm{pc}$;
4. the X-ray derived parameters do not exclude that the X-ray clumps are caused by thermal evaporation of shocked plasma in isolated clouds. An origin in terms of secondary shocks propagating in non-evaporative clouds is also consistent with the data. A forthcoming reduction of UV, optical photometric and spectrophotometric data on these shell region will help to detect more dense clouds and to shed light on the association between observations, on-going dynamical processes and ISM models.

Pursuing the correspondence between the hotter X-ray component and the inter-cloud medium, to which a Sedov analysis can be applied, we have found that:

1. the shell expansion occurs in a medium with a density of $0.03\,\mathrm{cm}^{-2}$;
2. the explosion energy of the supernova event, which gave rise to the SNR, was $\sim 1.2 \times 10^{50}$ erg, lower than previous estimate but in agreement with supernova models;
3. the derived distance is $\sim 280\,\mathrm{pc}$, in agreement with recent independent estimates;
4. very slight departures from instantaneous electron-ion energy equipartition are compatible with our data, but very slow equipartition (such as Coulomb collision) is to be excluded. Our results favour a fast equipartition behind the shock.

Finally, we have estimated the influence on our results of neglecting the possible NEI conditions of the shocked plasma. We found under reasonable assumptions the correction factors for the measured and derived parameters, and we argued that the differences do not affect our conclusions. The correction factors are not to be meant as a substitution for a full 2T NEI analysis, which will be feasible with higher spectral resolution detectors (SAX LECS/MECS, AXAF ACIS, XMM EPIC). The NEI analysis will also allow to address the crucial point of the plasma metal abundances, which cannot be afforded with *ROSAT* PSPC data.

Acknowledgements. F. Bocchino is grateful for stimulating discussions with J. Raymond at CfA in Cambridge, MA, USA, and with R. Bandiera at the Osservatorio Astrofisico di Arcetri, Italy. The authors wish to thank S. Serio, F. Reale and G. Peres for suggestions and comments. This work was supported by Ministero per l'Univerisita' e per la Ricerca Scientifica.

References

Asaoka I., Aschenbach B., 1994, A&A 284, 573
Aschenbach B., 1993, Adv. Space Res. 13, 1245
Aschenbach B., Brinkmann W., Pfeffermann E., Fuerst E., Reich W., 1991, A&A 246, L32

Bandiera R., Chen Y., 1994, A&A 284, 637
Bedogni R., Woodward W.R., 1990, A&A 231, 481
Bocchino F., 1997, Ph.D. Thesis, University of Palermo
Bocchino F., Maggio A., Sciortino S., 1994, ApJ 437, 209 (Paper I)
Bocchino F., Maggio A., Sciortino S., 1997, ApJ 481, 872 (Paper II)
Bocchino F., Barbera M., Sciortino S., 1998, A&AS 129, 647
Cargill P.J., Papadopoulos K., 1988, ApJ 329, 29
Charles P.A., Kahn S.M., McKee C.F., 1985, ApJ 295, 456
Cowie L.L., McKee C.F., 1977, ApJ 211, 135
Cowie L.L., McKee C.F., Ostriker J.P., 1981, ApJ 247, 908
Cox D.P., 1993, In: Cassinelli J.P., Churchwell E.B. (eds.) Massive Stars: Their Lives in the ISM. ASP Conf. Series 35, 402
Craig W.W., Hailey C.J., Pisarsky R.L., 1997, ApJ 488, 307
Cui W., Cox D.P., 1992, ApJ 401, 206
Dalton W.W., Balbus S.A., 1993, ApJ 404, 625
Decourchelle A., Sauvageot J.L., Ballet J., Aschenbach B., 1997, A&A 326, 811
Fürst E., Reich W., Aschenbach B., 1997, A&A 319, 655
Gorenstein P., Harnden R., Tucker W., 1974, ApJ 192, 661
Harrus I.M., Hughes J.P., Singh K.P., Koyama K., Asaoka I., 1997, ApJ 488, 781
Hester J.J., 1987, ApJ 314, 187
Hughes J.P., Singh K.P., 1994, ApJ 422, 126
Hwang U., Markert T.H., 1994, ApJ 431, 819
Itoh H., 1979, PASJ 31, 541
Jenkins E.B., Wallerstein G., 1995, ApJ 440, 227
Kahn S.M., Gorenstein P., Harnden F.R., Seward F.D., 1985, ApJ 299, 821
Korpela E.J., Bowyer S., Edelstein J., 1998, ApJ 495, 317.
Ku W.H.-M., Kahn S.M., Pisarski R., Long K.S., 1984, ApJ 278, 615
Laming J.M., Raymond J.C., McLaughlin B.M., Blair W.P., 1996, ApJ 472, 267
Landau L.D., Lifshitz E.M., 1974, Fluid Mechanics. Pergamon Press
Lattimer J.M., Burrows A., Yahil A., 1985, ApJ 288, 644
Lesch H., 1990, A&A 233, 417
Milne D.K., 1968, AusJP 21, 201
Masai K., 1994, ApJ 437, 770
McKee C.F., 1974, ApJ 188, 335
McKee C.F., Cowie L.L., 1975, ApJ 195, 715
McKee C.F., Hollenbach D.J., 1980, ARA&A 18, 219
McKee C.F., Ostriker J.P., 1977, ApJ 218, 148
Nomoto K., Sugimoto D., Neo S., 1976, Ap&SS 39, L37
Oberlack U., Diehl R., Montmerle T., Prantzos N., von Ballmoos P., 1994, ApJS 92, 433
Pfeffermann E., Aschenbach B., Predehl P., 1991, AA 246, L28
Raymond J.C., Smith B.W., 1977, ApJS 35, 419
Seward F.D., 1990, ApJS 73, 781
Shelton R.L., Cox D.P., 1994, ApJ 434, 599
Slavin J.D., Cox D.P., 1993, ApJ 417, 187
Snowden S.L., McCammon D., Burrows D.N., Mendenhall J.A., 1994, ApJ 424, 714
Spitzer L., 1962, Physics of Fully Ionized Gases. Interscience, New York
Taylor J.H., Manchester R.N., Lyne A.G., 1993, ApJS 88, 529
Trümper J., 1983, Adv. Space Res. 4, 241
Weiler K.W., Panagia N., 1980, A&A 90, 269
Weiler K.W., Sramek R.A., 1988, ARA&A 26, 295
White R.L., Long K.S., 1991, ApJ 373, 543
Willingale R., West R.G., Pye J.P., Stewart G.C., 1996, MNRAS 278, 749
Yamauchi S., Ueno S., Koyama K., et al., 1993, PASJ 45, 795